Advances in Geo-Energy Research

Vol. 13, No. 2, p. 146-160, 2024

Original article

Identification and parameter characterization of pores and fractures in shales based on multi-scale digital core data

Ying Zhou[1,2,3], Xiaoqin Zhong[3,4], Xin Nie[1,2,3]*

[1]*Cooperative Innovation Center of Unconventional Oil and Gas, Yangtze University (Ministry of Education & Hubei Province), Wuhan 430100, P. R. China*

[2]*Key Laboratory of Exploration Technologies for Oil and Gas Resources, Yangtze University, Wuhan 430100, P. R. China*

[3]*National Engineering Laboratory for Exploration and Development of Low-Permeability Oil & Gas Fields, Xi'an 710018, P. R. China*

[4]*Exploration and Development Research Institute, PetroChina Changqing Oilfield Company, Xi'an 710018, P. R. China*

Keywords:
Digital core
pore identification
pore structure
fracture attitude
unconventional reservoirs

Cited as:
Zhou, Y., Zhong, X., Nie, X. Identification and parameter characterization of pores and fractures in shales based on multi-scale digital core data. Advances in Geo-Energy Research, 2024, 13(2): 146-160.
https://doi.org/10.46690/ager.2024.08.08

Abstract:
Accurate pore structure characterization, as a basic tool for efficient exploration and development in reservoirs and digital rock, has become increasingly popular nowadays. However, using single-scale digital core data, it is difficult to evaluate the multi-scale pore structures in shales. This study proposes an integrated workflow for identifying and extracting pore parameters from multi-scale three-dimensional and two-dimensional digital rock images, which includes full-diameter core computed tomography (CT), micro-CT, focused ion beam-scanning electron microscopy and scanning electron microscopy images. This workflow realizes the identification and parameter extraction of pores and fractures from mesoscopic to microscopic scales. First, meso-fractures are extracted using the connected domain analysis method from full-diameter CT images, and the apparent attitudes are calculated using the least squares and connected domain analysis method. Then, micropores and fractures are identified from Micro-CT and focused ion beam-scanning electron microscopy data, and the pore network models are established. Features, including pore radius, surface area, volume, throat radius, length, and coordination number, are calculated based on the maximum ball method. Different types of pores in scanning electron microscopy images are automatically identified using deep learning methods, and the pore parameters are computed using connected domain analysis methods. Subsequently, the workflow is applied to a practical case and the results show accurate extractions of pore structure information. This study provides important guidance and support for the quantitative evaluation of pores and fractures in unconventional reservoirs.

1. Introduction

Shale reservoirs exhibit a complex pore structure with pronounced heterogeneity, where the pore size is widely distributed across the micro- and nanoscales (Slatt and O'Brien, 2011; Iqbal et al., 2021; Li et al., 2024). The variety of pores and fractures in organic matter and minerals constitute an important path for oil and gas storage and migration (Loucks et al., 2009). Therefore, the qualitative and quantitative characterization of the multi-scale pore structure is vital for reservoir prediction and the enhancement of production capacity (Josh et al., 2019; Kumar et al., 2019).

The commonly used pore structure characterization methods are based on fluid injection, non-fluid injection, or imaging (Mastalerz et al., 2017, 2021; Li et al., 2023a, 2023b). The latter utilize high-resolution imaging techniques such as scanning electron microscopy (SEM) to scan samples to

Yandy Scientific Press

*Corresponding author.
E-mail address: zfg18711@163.com (Y. Zhou); zhongxiaoqin_cq@petrochina.com.cn (X. Zhong); niexin_cugb@126.com (X. Nie).

Received May 30, 2024; revised June 27, 2024; accepted July 24, 2024; available online August 1, 2024.

identify pores and fractures within the cores, followed by quantitative characterization (Kwiecińska et al., 2019; Valentine and Hackley, 2023). This kind of approach has the advantages of low cost, high precision and repeatability, which have made it popular in the analysis of microscopic pore structure of shale reservoirs. Accordingly, many scholars have implemented imaging methods to study the pore structure of shale reservoirs from different scales.

Micro- and nanopores are important for gas storage in shale reservoirs. A lot of research has focused on the characterization of such pore structures. SEM as the most prevalent two-dimensional (2D) scanning technique offers nano-scale accuracy suitable for characterizing the micro-scale storage space in shale formations. Other 2D techniques employed for micro-nanopore structure characterization include modular automated processing system, transmission electron microscopy, and atomic force microscopy, or three-dimensional (3D) scanning techniques such as computed tomography (CT), focused ion beam scanning electron microscopy (FIB-SEM), etc. (Goral and Deo, 2020; Guo et al., 2022; Masihi et al., 2022; Yalamanchi and Datta Gupta, 2024).

Researchers typically utilize threshold segmentation methods to identify pores in core images (Schlüter et al., 2014; Gobert et al., 2020). Furthermore, machine learning and deep learning have been gradually applied to image classification tasks and shown outstanding performance (Badrinarayanan et al., 2017; Saxena et al., 2021; Gao et al., 2023; Roslin et al., 2023). Among them, the pixel-wise semantic segmentation network model is favored by many researchers and is commonly used in pore identification. The main network models are classical models such as FCN, U-Net and U-Net++. The U-Net model, one of the most popular convolutional neural networks (CNNs), was developed based on FCN. It improves the ability of feature acquisition by connecting encoders and decoders through skip connections (Ronneberger et al., 2015; Shelhamer et al., 2017). With the expansion of image segmentation to a growing number of fields, a variety of variants based on the U-Net network have been proposed to address problems such as pore recognition (Byun et al., 2021), multi-component core modeling (Li et al., 2022), and fluid flow prediction (Jiang et al., 2021).

For shale reservoirs, the development of mesoscopic-scale fractures significantly affects large-scale oil production (Mukherjee and Vishal, 2023). At present, the research on mesoscopic-scale fractures mainly targets fracture identification (Wei et al., 2023) and prediction (Ou and Li, 2017). Fracture identification mainly relies on core observation and imaging logging methods (Nie et al., 2013; Yin et al., 2022). These observations help to describe fracture density and geophysical morphology but cannot quantify fracture parameters in 3D space, and thus fails to effectively evaluate the oil and gas exploitation potential.

Pores and fractures at both meso- and microscales are important in shale reservoirs. Therefore, it is crucial to quantitatively assess multi-scale pore development in these reservoirs. However, former studies only focused on the identification and parameter extraction of pores at a single scale, while little research has been conducted on multi-scale pore characterization from meso- to nanoscales. To address this shortcoming, this study combines multi-scale and multi-dimensional pore characterization methods and proposes an integrated workflow for identifying pores and fractures and extracting their parameters based on digital core images derived from multi-scale images, including full-diameter core CT, micro-CT, FIB-SEM, and SEM images. The developed workflow is applied to process actual data from the TY field. This paper effectively characterizes meso-microscale pores and fractures within the reservoir, guiding the effective exploration and development of shale reservoirs.

2. Methods

2.1 Identification and parameter extraction of mesoscopic fractures

Mesoscopic fractures in CT images of full-diameter cores are automatically picked up based on a connected domain analysis method. Fig. 1 shows the fracture extraction process, including image binarization, trimming and inversion. As shown in Fig. 1(a), the irregular black horizontal-like area inside the core is a fracture. After binarization, the core image is divided into two parts (Fig. 1(b)), with the black area close to the level being the fracture and the remaining white area being the mineral matrix or other rock components. Fig. 1(c) presents the CT image of the core after trimming. Finally, the image is subjected to an inverse operation to obtain the data containing fractures (white) and the matrix (black) (Fig. 1(d)).

Based on the extracted fractures, the least square method is used to extract the apparent attitude of fractures (Zhou et al., 2023). In Fig. 2, the blue rectangles represent orthogonal 2D planes; the inclined ellipse P represents the actual fracture plane; the four black dots represent the characteristic points of the fracture in the orthogonal plane; the letter v represents the normal vector of the plane; φ indicates the fracture's apparent dip angle; the letter v' represents the projection vector of the normal vector; and θ indicates the fracture's apparent dip direction. The parameters such as fracture density are obtained by connected domain analysis.

2.2 Identification and parameter extraction of 3D micro-nanopores and fractures

Micro-CT images usually have noise and artifacts. A large number of previous studies have shown that median filtering performs well in dealing with class problems. Therefore, the median filtering and the unsharp masking method (USM) is selected to eliminate the noise and enhance the image contrast. Fig. 3(a) shows the original slice of B1, while Figs. 3(b) and 3(c) depict the image after median filtering and unsharp masking, respectively.

In FIB-SEM, the vertical stripe on the slice is often referred to as the "curtain effect". The grayscale of these stripes is close to that of pores, which will affect the accuracy of pore extraction. To reduce the effect of similar periodic noise, the Fast Fourier transform filter is applied to the image. Fig. 4 illustrates the process of eliminating the "curtain effect". Fig. 4(a) shows the original FIB-SEM slice and Fig. 4(b) shows

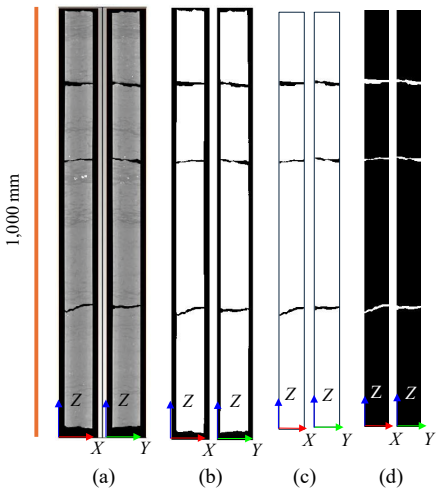

Fig. 1. Automatic extraction process of fractures from full-diameter core CT. (a) Original image, (b) binarized image, (c) cropped image and (d) inverted image.

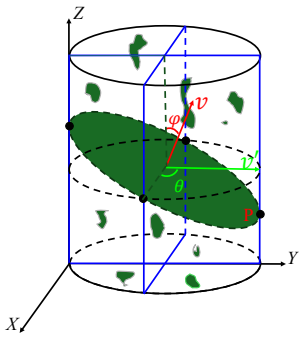

Fig. 2. The principle of fracture apparent attitude was extracted based on the least square method.

the slice image filtered by Fast Fourier transform filter, in which the vertical stripe artifacts are successfully eliminated. Subsequently, the USM method is used to enhance edge information in the images (see Fig. 4(c)).

After data pre-processing, threshold segmentation is utilized in pore and fracture identification. The micro-CT and FIB-SEM data selected were stored in 8-bit format and the image grayscale distribution was between 0 and 255. In the image, the grayscale value of 0 is shown in black, and 255 is shown in white. A suitable threshold is selected to divide the pores and the matrix, and a pore network model is established based on the extracted pores using the maximum ball algorithm (Dong and Blunt, 2009), which can finely characterize the internal pore throat structure of the core.

Based on the pore network model, the parameters of the pores are calculated, including pore radius, coordination number, throat radius, and throat length. Fig. 5 shows a schematic diagram of the division of the pore and the throat based on the maximum ball:

1) Pore radius: It is defined as the radius of the maximal ball r_i.
2) Coordination number: It is defined as the number of throats connected to the pores, which can reflect the 3D connectivity of pore space; the higher the coordination number, the better the pore connectivity and the better the reservoir properties.
3) Throat radius: It is the radius of the ball of the throat r_t.
4) Throat length: It is the length of the throat connecting the two largest balls between them, i.e., the difference between the distance from pore i to the center of mass of pore j and the sum of the radii of both.

$$L = l_{ij} - r_i - r_j \tag{1}$$

2.3 Identification and parameter extraction of 2D nanopores and fractures

In recent years, CNNs have performed well in image segmentation tasks. Increasingly more experts and academics have used CNNs to identify pores and fractures in digital core images with excellent results. Here, the U-Net++ network model is used to identify the pores and fractures in SEM images, then the parameter of the pores and fractures is extracted by image analysis. The workflow contains three main parts: dataset creation, pore-fracture identification, and parameter extraction.

2.3.1 Dataset creation

After screening, 53 original SEM images are selected from the dataset. Before labeling the image, the non-local means filtering method is selected to eliminate the noise in the SEM image, and the USM algorithm is used to enhance the contrast of the image. The pre-processed image is shown in Fig. 6, along with the original image, the filtered image, and the image after image enhancement.

Image labeling is a crucial step in creating the training dataset. Here, the images are labeled with the help of ImageJ. After importing the SEM image, the pores are manually labeled, and the labeled image will be generated and combined with Weka Segmentation. The labeled image contains four labels : Organic pore, inorganic pore, fracture, and skeleton, which are displayed as red, yellow, green, and black in the label image, and the label values are 0, 1, 2 and 3.

The size of the training dataset is crucial for the performance and generalization ability of deep learning models: A larger training dataset can provide more sample information, which in turn helps the model learn more accurate features. The dataset is expanded by cropping and rotation. As shown in Fig. 7, the original images are cropped into subsamples using a sliding window of 256×256 pixels in size, and some of the images are randomly selected and rotated by 180°. Finally, a total of 562 SEM images are obtained.

The dataset is divided into two parts: Training set and validation set at an approximate 9:1 ratio, which mean 500 and 62 images, respectively.

2.3.2 Identification of pores and fractures

U-Net++ is a network model that improves on the U-Net model. The main difference between the two is the way skip connections are handled. In the basic U-Net model, skip conn-

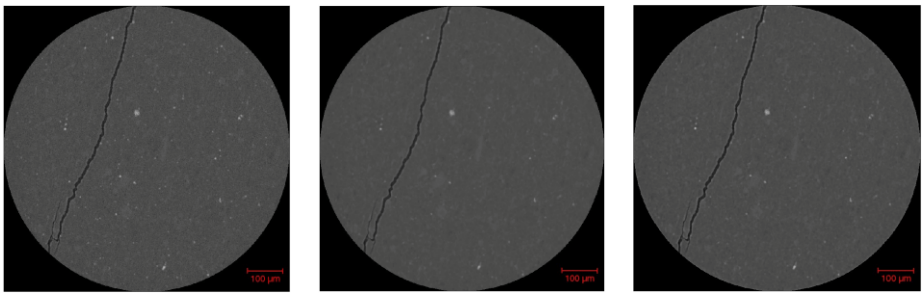

(a) (b) (c)

Fig. 3. Pre-processing of the micro-CT. (a) Original image, (b) filtered image and (c) enhanced image.

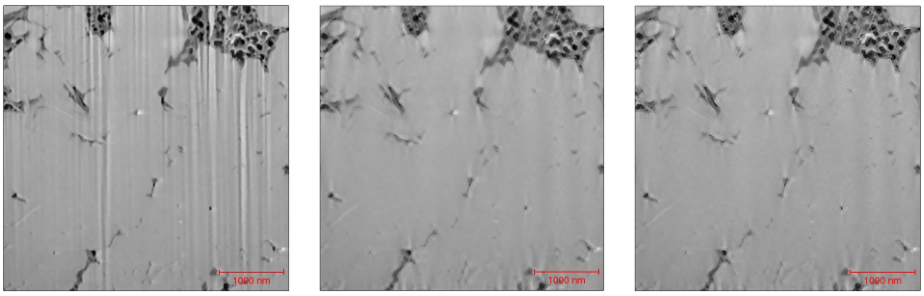

(a) (b) (c)

Fig. 4. Pre-processing of FIB-SEM. (a) Original image, (b) filtered image and (c) enhanced image.

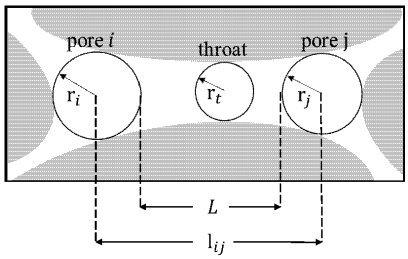

Fig. 5. Partition of pore and throat based on the maximum ball algorithm.

ections pass and connect features directly from the encoder part to the decoder part. In contrast, in the U-Net++ model, a dense skip-connection path is used in which features are passed through a varying number of intermediate blocks. These blocks are connected to all previous blocks at the same level through a tandem layer (Fig. 8). This dense skip connection path provides more feature information transfer and utilization and helps to improve the model performance.

During the training process, the learning rate is set to 0.001, the batch-size is set to 32, and the epoch is set to 250 times. Fig. 9 shows the loss of the training set and the validation set.

After the model training process, the SEM image is input into the trained network model and the predicted image is obtained by forward propagation.

2.3.3 Parameter extraction

The images output by the deep learning network model are segmented into organic pore, inorganic pore, fracture and skeleton. By calculating the fundamental parameters of the ellipse having the same second-order moments as the connected domain (Fig. 10), the different pore parameters such as pore radius, aspect ratio, shape factor, and areal porosity of different types of pores are obtained.

1) Pore radius
The pore radius (r) is the length of the short axis of the ellipse.

$$r = b \tag{2}$$

where b denotes the short axis of the ellipse.

2) Aspect ratio
Aspect ratio (a_r) is defined as the ratio of the short axis to the long axis of the ellipse, which is distributed between 0 and 1. The pores with a_r close to 1 are circular.

$$a_r = \frac{b}{a} \tag{3}$$

where a is the long axis of the ellipse.

3) Shape factor
The pore shape factor (G) is obtained by Eq. (4). It characterizes the degree of regularity of the pore shape, and the closer the shape factor is to 1, the more regular the 2D morphology.

$$G = \frac{4\pi S}{C^2} \tag{4}$$

where S represents the sum of the areas of all pixel points in the connectivity domain, and C is the perimeter.

4) Areal porosity

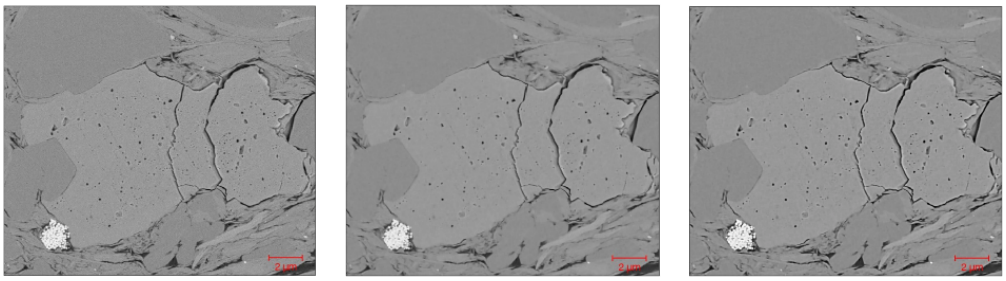

(a) (b) (c)

Fig. 6. Pre-processing of SEM. (a) Original image, (b) filtered image and (c) enhanced image.

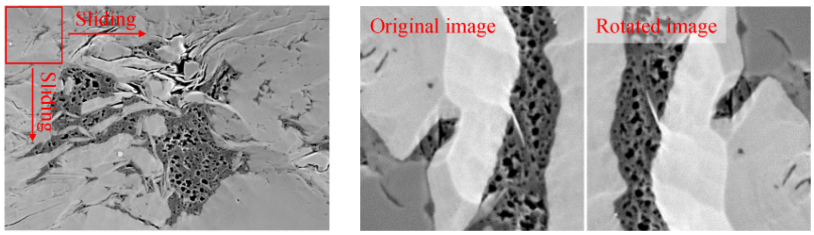

(a) (b)

Fig. 7. Data augmentation. (a) Image cropping and (b) image rotation

Areal porosity (ϕ) is one of the basic pore parameters in the SEM image analysis of pore structure parameters, calculated as shown in Eq. (5):

$$\phi = \sum_{i=1}^{n} \frac{S_i}{S_t} \times 100\% \tag{5}$$

where n indicates the number of the pore, S_i represents the area of pore i , and S_t is the area of the whole image.

2.4 Integrated workflow

By combining the methods mentioned above, an integrated workflow for multi-scale data processing, encompassing full-diameter core CT, micro-CT, and FIB-SEM and SEM images of varying scales, is presented (Fig. 11). This process facilitates mesoscopic to microscopic and 3D to 2D characterization and the parameter extraction of pore structures.

3. Application and results

3.1 Data collection

In order to verify the applicability of the proposed workflow, 318 m of full-diameter core CT, 9 sets of micro-CT, 9 sets of FIB-SEM, and 5 sets of SEM data of the Wufeng-Longmaxi Formation in the TY gas field were selected to characterize pore structure from mesoscopic to nanoscopic. The Longyi Formation is hereinafter referred to as Long1.

The selected full-diameter core CT images were obtained by dual-energy CT scanning. Micro-CT images were obtained by the X-CT method using a Versa XRM-500 scanner with a resolution of 1 μm. FIB-SEM and SEM images were obtained by Helios NanoLab 650 FIB / SEM dual-beam scanning electron microscope. The detailed information of samples is shown in Tables 1-4.

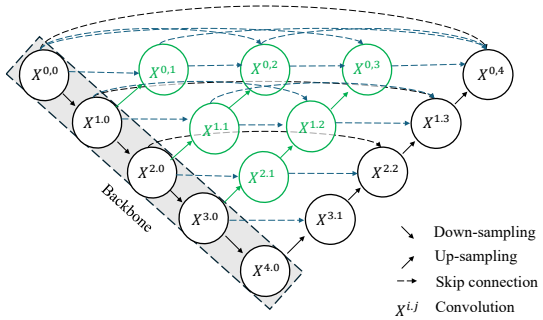

Fig. 8. Structure of the U-Net++ model.

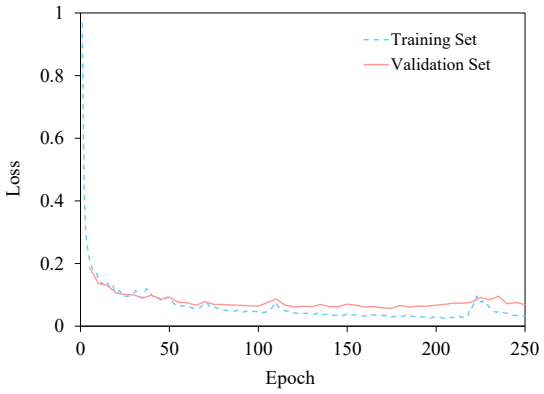

Fig. 9. Change of loss on the training set and validation set during network training.

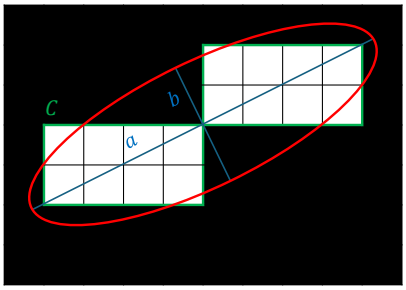

Fig. 10. Extraction of basic pore parameters.

Table 1. Information of full-diameter core CT data.

Well	Formation	Length (m)
A11	$Long1_2$~Wufeng	115
B104	$Long1_2$~Wufeng	95
C118	$Long1_1^4$~Wufeng	29
C206	$Long1_1^3$~Wufeng	24
C207	$Long1_2$~Wufeng	55

3.2 Mesoscopic fractures in full-diameter core CT

Using the workflow proposed in this paper, the fractures of full-diameter core CT are quickly and automatically extracted, and parameters such as fracture apparent attitude, fracture density, etc. are rapidly determined based on the least-squares method and connected-domain analysis. The extracted fracture parameters are shown in Table 5. Fig. 1 demonstrates a process of mesoscopic fracture identification.

According to the results for the 318 m full-diameter core CT image of 5 wells in the TY gas field, the horizontal low-angle fractures are widely developed, with an occasional occurrence of high-angle fractures. As shown in Fig. 12, the development of low-angle fractures in the Longmaxi Formation has strong heterogeneity. For example, in $Long1_1^3$, the density of the fracture in well C118 is 13.33 fractures/m, and that in well C207 is 5.6 fractures/m; the density in well A11 of Wufeng Formation is 12.1 fractures/m, and that in well C207 is 3.33 fractures/m. The development of high-angle fractures in wells A11 and C207 is relatively high, but there are no obvious features.

Mesoscopic fractures in the Wufeng-Longmaxi Formation in the study area are relatively developed; most of the fractures' opening are between 1 and 10 mm. The differences in the vertical and horizontal development of fractures were analyzed (Fig. 12). Vertically, the development of mesoscopic fractures in different layers varies greatly, and the $Long1_1^1$ has more developed low-angle fractures. The density of fractures in the $Long1_1^1$ sub-layer is the highest, all wells reaching more than 10 fractures/m. The density of fractures in the Wufeng Formation is lower than that in the Longmaxi Formation. Horizontally, the fracture development of different wells in the same layer varies; the fracture density of well A11 is higher than other wells.

3.3 3D micro-nano pores and fractures in micro-CT and FIB-SEM

3.3.1 Micro-pores and fractures in micro-CT

(1) Identification of pores and fractures.

Firstly, the CT image is pre-processed by median filtering and unsharp masking. Then, the pores and fractures are extracted by threshold segmentation, while the pore network model is established using the maximum ball algorithm. In the 3D pore network model, a sphere is used to represent the pore and a stick is used to represent the throat, while the different colors represent the pore or the throat of different radii. The larger the pore radius, the closer the color of the sphere is to red, and the smaller the pore radius, the closer the color of the sphere is to blue. The throat is rendered based on the same principle, as can be observed from Fig. 13.

The number of small pores in the pore network model extracted from the 9 samples is relatively high. It can be observed that sample A3 develops a low-angle fracture and some micropores. At the same time, there is a Z-direction penetrating fracture and a few isolated pores in sample B1, while B3 contains a few microfractures and a few micropores. C6 contains a vertically oriented fracture; cluster pores are developed in samples B12 and Z15; samples D6 and Z3 contain a few pores with large pore radius; whereas only a few micropores developed in sample Z8.

(2) Parameter extraction.

For the representative samples selected from different layers, a pore network model is established to extract the pore parameters. In Table 6, the porosity (ϕ), pore number (n), average pore radius (r_m), average surface area (A_m), average volume (V_m), average throat length (l_t), average throat radius (r_t), average coordination number (C_m), and connectivity pore ratio (p_c) are calculated.

Among the samples, Z15 has the largest porosity, which is characterized by the development of clustered pores, and the average coordination number is 4. B1 has the largest proportion of connected pores to total pore volume, which is mainly due to the development of fractures and fewer isolated pores in the sample. The average pore radius of sample B1 is 5.31 μm, and that of the others cores is less than 5 μm. The average coordination number is 5, indicating better pore connectivity.

At the current scanning resolution, the organic matter pores cannot be observed, and most of the extracted pores are inorganic pores. In fact, in shale reservoirs, although some micro-scale pores are isolated from each other, nano-scale pores are interconnected and are important sites and paths for oil and gas storage and migration. Therefore, combined with FIB-SEM, the nano-scale pore structure is further analyzed in detail.

3.3.2 Nanopores and fractures in FIB-SEM

(1) Identification of pores and fractures.

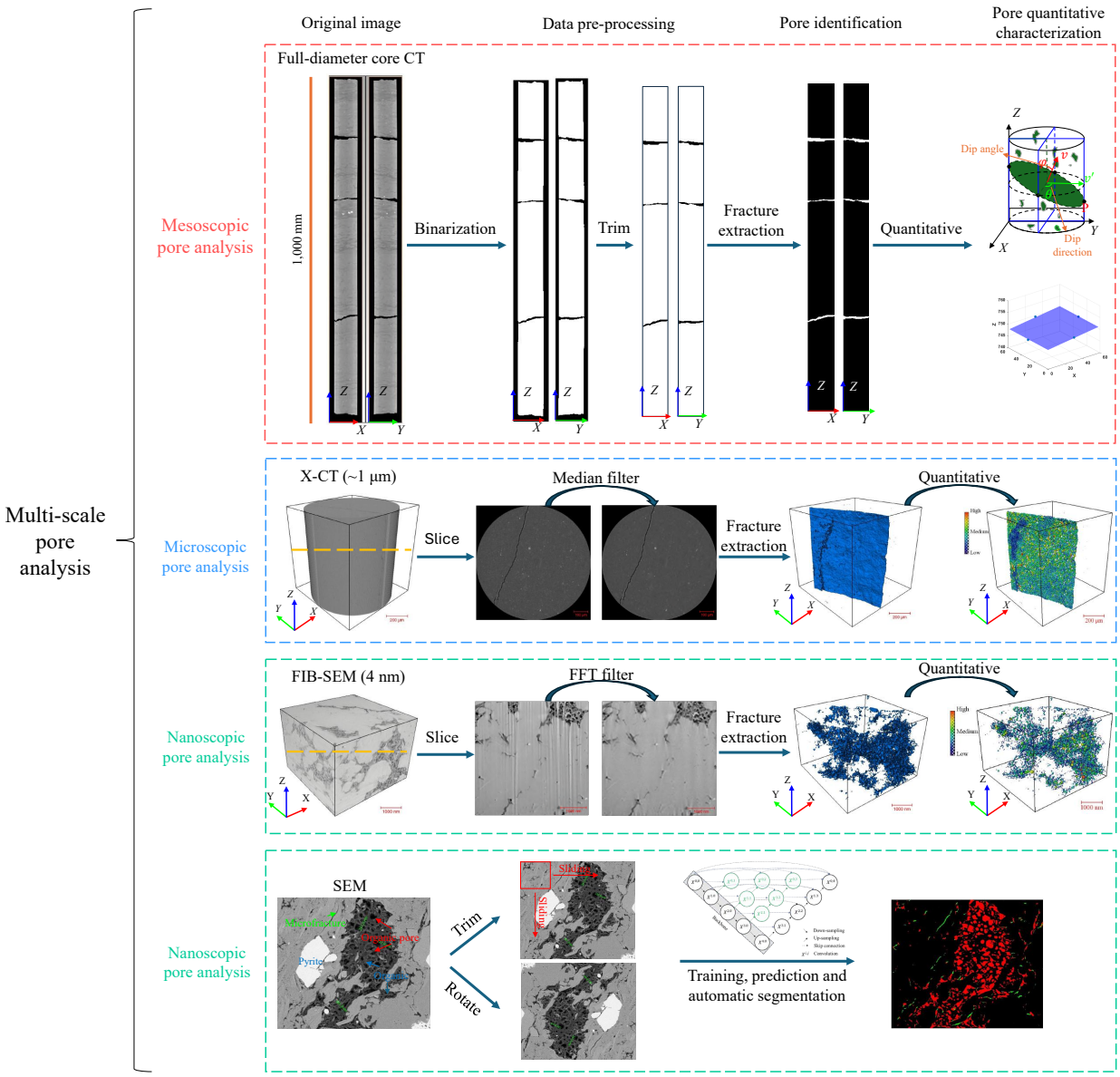

Fig. 11. Flow chart of multi-scale pore identification and parameter extraction of shale.

Table 2. Information of micro-CT data.

No.	Formation	Image size (voxel)	Real size (μm)
B1	$Long1_2$	$800 \times 800 \times 800$	$802.685 \times 802.685 \times 802.685$
Z15	$Long1_1^4$	$936 \times 1016 \times 900$	$748.37 \times 812.402 \times 719.556$
A3	$Long1_1^3$	$800 \times 800 \times 800$	$802.047 \times 802.047 \times 802.047$
B3	$Long1_1^2$	$800 \times 800 \times 800$	$800.569 \times 800.569 \times 800.569$
Z8	$Long1_1^2$	$944 \times 1016 \times 800$	$754.774 \times 812.402 \times 639.517$
B12	$Long1_1^1$	$800 \times 800 \times 800$	$799.637 \times 799.637 \times 799.637$
Z3	$Long1_1^1$	$936 \times 1016 \times 995$	$748.37 \times 812.402 \times 795.594$
D6	Wufeng	$800 \times 800 \times 800$	$801.081 \times 801.081 \times 801.081$
C6	Wufeng	$800 \times 800 \times 800$	$799.637 \times 799.637 \times 799.637$

Table 3. Information of FIB-SEM data.

No.	Formation	Image size (voxel)	Real size (μm)
B1	$Long1_2$	$1,200 \times 1,200 \times 600$	$4.8 \times 4.8 \times 2.4$
Z15	$Long1_1^4$	$1,200 \times 1,200 \times 900$	$4.8 \times 4.8 \times 3.6$
C1	$Long1_1^3$	$1,000 \times 1,000 \times 500$	$4 \times 4 \times 2$
B3	$Long1_1^2$	$1,100 \times 1,100 \times 750$	$4.4 \times 4.4 \times 3$
B9	$Long1_1^2$	$1,100 \times 1,100 \times 800$	$4.4 \times 4.4 \times 3.2$
D4	$Long1_1^1$	$1,000 \times 1,000 \times 500$	$4 \times 4 \times 2$
B12	$Long1_1^1$	$1,100 \times 1,100 \times 750$	$4.4 \times 4.4 \times 3$
D6	Wufeng	$1,200 \times 1,100 \times 800$	$4.8 \times 4.4 \times 3.2$
C6	Wufeng	$1,200 \times 1,200 \times 600$	$4.8 \times 4.8 \times 2.4$

Table 4. Information of SEM data.

No.	Formation	Image size (pixel)	Real size (μm)
135-1	$Long1_2$	576×480	27.16×22.64
136-3	$Long1_2$	640×544	21.58×19.31
135-2	$Long1_1^4$	608×512	7.89×6.65
11-6	$Long1_1^3$	640×544	21.58×19.31
11-8	$Long1_1^2$	640×544	21.58×19.31

Table 5. Fracture parameters of full-diameter core CT.

No.	Fracture	Density (Fracture/m)	Aperture (mm)	Dip angle (°)	Dip direction (°)
1	1	3	3.52	2.21	205.9
	2	3	1.78	6.3	234.8
	3	3	2.07	2.97	179.7
2	1	1	3	8.2	164.2
4	1	1	7.46	1.78	201.5

In the FIB-SEM, the distribution of organic matter and pores can be observed. In the study area, organic pores are more developed in most samples, while inorganic pores are scarce. Pre-processing of FIB-SEM is conducted using fast Fourier transform and unsharp masking. Threshold segmentation is employed to extract pores and fractures, revealing the distribution of nano-scale pores in the sample. Subsequently, the pore network model is established and relevant pore parameters are obtained. Fig. 14 presents the pore network model of the samples, where pores and throats of different radii are represented by different colors.

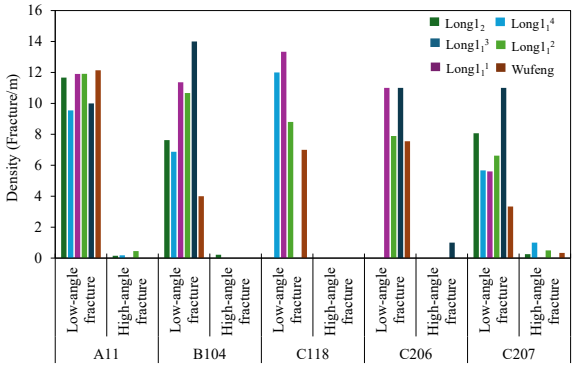

Fig. 12. Fracture density in different wells and formations.

There are a few inorganic pores observed at the nanoscale, while organic pores are widely developed. The distribution of most micropores in the FIB-SEM exhibits consistency, primarily composed of a network of larger organic pores and some isolated pores. Consistent with previous research, organic pores are observed to be interconnected in 3D space, serving as the main structural component of the connected pore network (Wu et al., 2020).

(2) Parameter extraction.

After establishing the pore network model using the maximum ball algorithm, the pore parameters can be calculated. Nine sets of pore parameters extracted from the sample are presented in Table 7.

Among the results, sample B12 exhibits the highest porosity at 4.26%. Organic pores in the sample are clustered, which demonstrates the best pore connectivity. The average coordination number is 2, and the connected pore volume accounts for 87.49% of the total pore volume. In contrast, the porosity of sample B1 is the lowest, only 0.01%, and the proportion of connected pore volume to total pore volume is the smallest at 27.21%.

3.4 2D nanopores and fractures in SEM

The U-Net++ was employed to identify different types of pores in SEM images. The SEM images were input into a pre-trained neural network model for image segmentation, allowing for the extraction of different types of pores. Fig. 15 illustrates the pore and fracture identification results of the SEM images. In the predicted image, organic pores, inorganic pores and microfractures are represented by red, yellow and green, respectively.

After extracting different types of pores using the U-Net++ model, the characteristic parameters of organic and inorganic pores obtained through connected domain analysis are presented in Tables 8 and 9, respectively, which include pore number (n), areal porosity (ϕ), average radius (r_m), aspect ratio (a_r), shape factor (G), and proportion of total areal porosity (ϕ_o, ϕ_i).

The pores of organic matter in the study area are mainly in the form of near circular, oval and slit. As observed in 135-1 and 136-3 samples, the intragranular pores are mainly circular. The pore shape of intergranular pores is diverse. The pore diameter of the organic pores is mainly distributed in the range of 50-700 nm, and the pore diameter of some organic

Table 6. Pore and throat parameters of micro-CT.

No.	ϕ (%)	n	r_m (μm)	A_m (μm^2)	V_m (μm^3)	l_t (μm)	r_t (μm)	C_m	p_c (%)
B1	0.81	4,317	5.31	580.30	977.35	3.53	15.52	5	99.62
Z15	2.17	27,746	3.54	286.67	269.34	1.85	11.11	4	94.46
A3	0.31	11,730	2.17	153.73	142.74	2.21	14.16	1	84.09
B3	0.28	2,710	4.46	446.88	530.84	2.32	13.77	4	77.98
Z8	0.37	9,246	2.50	127.08	82.98	1.20	6.76	3	25.50
B12	1.05	4,784	4.27	392.04	447.67	2.21	12.97	2	70.07
Z3	1.07	10,480	3.33	230.96	205.74	1.60	9.79	2	58.71
D6	1.01	18,340	3.27	201.97	196.49	1.70	9.01	1	28.12
C6	0.90	13,104	3.63	264.27	269.74	2.10	11.32	3	61.42

Table 7. Pore and throat parameters of FIB-SEM.

No.	ϕ (%)	n	r_m (nm)	A_m (nm^2)	V_m (nm^3)	l_t (nm)	r_t (nm)	p_c (%)
B1	0.01	44	13.16	5,100	29,993	44.74	15.28	27.21
Z15	0.15	8,750	6.67	2,337	14,437	50.69	10.95	60.49
C1	0.21	2,281	9.78	3,938	30,080	47.84	11.23	43.25
B3	0.42	5,748	11.30	5,407	42,418	59.55	12.43	76.55
B9	1.58	18,487	13.61	6,630	53,156	58.18	11.58	71.04
D4	0.58	4,143	12.44	5,701	44,906	57.54	12.08	59.20
B12	4.26	59,160	12.79	5,605	35,542	53.74	9.27	87.49
D6	0.94	59,158	6.85	2,119	10,736	44.57	8.97	72.57
C6	0.52	4,939	14.62	7,357	59,120	59.03	13.05	48.96

pores reaches 1,000 nm or larger (see Fig. 16). The inorganic pore diameter is mainly distributed between 50-600 nm, and some of the pore diameters reach 800 nm.

In general, the inorganic pores of samples 135-1 and 136-3 from Long1_2 are more developed. Samples 135-2 and 135-1 were taken from the same well and sample 135-2 was taken from the Long$1_1{}^4$ layer. In contrast, the organic pores are more developed and the pore diameter is larger. Samples 11-6 and 11-8 taken from different layers of the same well show different pore characteristics, the sample 11-8 of Long$1_1{}^2$ has a large diameter of organic pore, and sample 11-6 mainly develops microfractures.

4. Discussion

4.1 Comparison of pore identification methods

This study introduces an innovative integrated multi-scale digital core image processing workflow aimed at identifying and quantitatively characterizing pores and fractures across various imaging modalities: full-diameter core CT, micro-CT, FIB-SEM, and SEM. For pore and fracture identification, diverse methodologies are employed: mesoscopic-scale fractures are detected using the connected domain analysis method (Zhou et al., 2023); 3D micro-nanopores and fractures are segmented via threshold segmentation (Liu et al., 2023). For pore and fracture parameters extraction: the mesoscopic-scale fractures' apparent attitude is extracted using the least square method (Zhou et al., 2023); 3D micro-nanopores and fractures parameters are obtained via the maximal ball algorithm (Dong and Blunt, 2009); and 2D nano-scale pores and fractures parameters are extracted using the connected domain analysis method. These methods mentioned above have practically proven as efficient and accurate and have been thoroughly discussed in the original references. Therefore, in this part, the identification method for 2D nano-scale pores and fractures will be mainly discussed.

In this paper, 2D nano-scale pores and fractures are identified using the U-Net++ network structure. In terms of addressing different pore recognition challenges, pixel-level semantic segmentation networks demonstrate robust performance. Mean Intersection over Union (MIoU) is a commonly used metric for evaluating the performance of segmentation models. It measures the accuracy of the model's predictions by calculating the Intersection over Union (IoU) for each class, where IoU represents the ratio of the intersection to the union between the predicted regions and the ground truth labels. The average IoU across all classes yields the MIoU. The formula

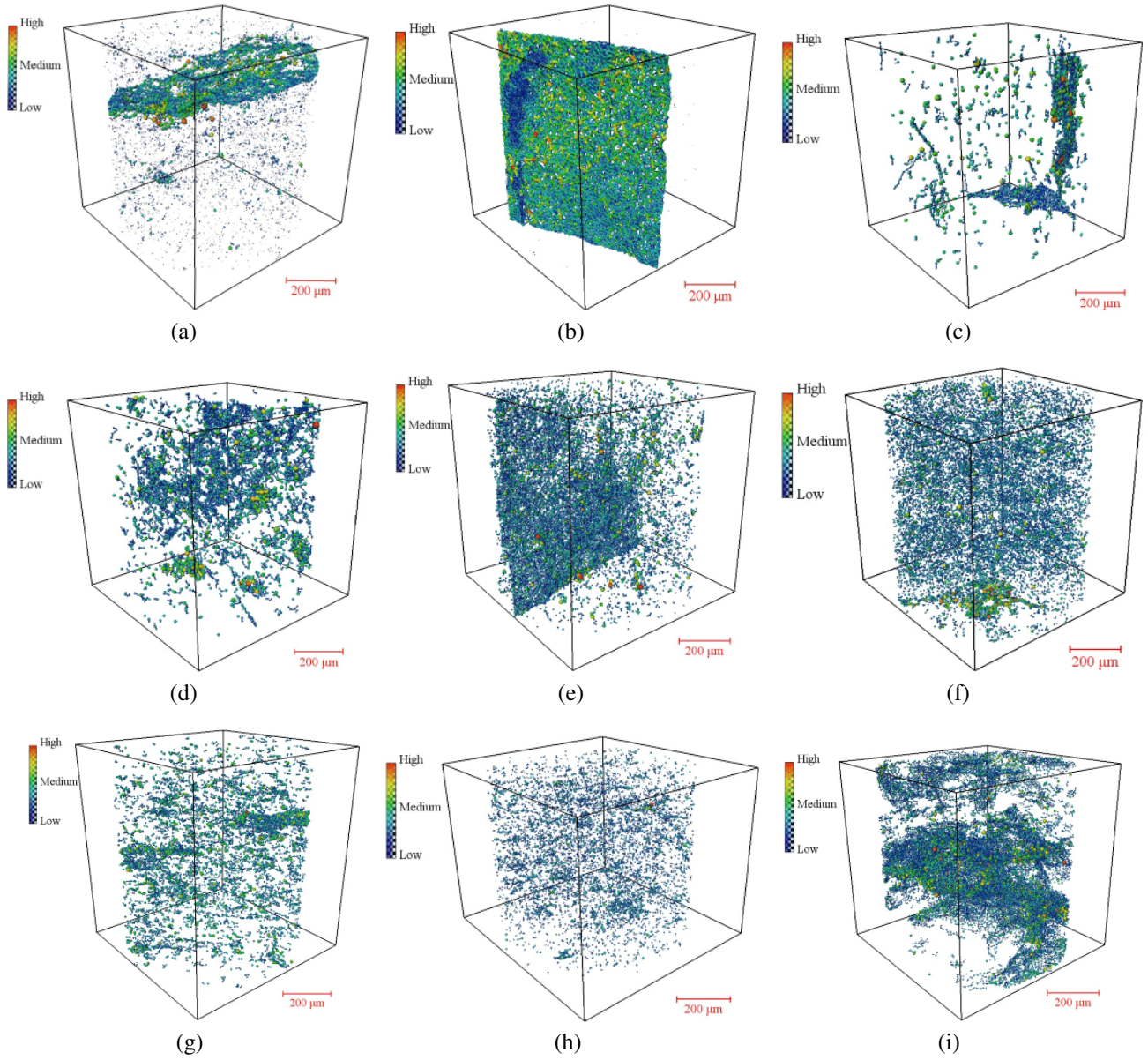

Fig. 13. Pore network model of micro-CT. (a) A3, (b) B1, (c) B3, (d) B12, (e) C6, (f) D6, (g) Z3, (h) Z8 and (i) Z15.

for computation is as follows:

$$\mathrm{MIoU} = \frac{1}{k+1}\sum_{i=0}^{k}\frac{p_{ii}}{\sum_{j=0}^{k}p_{ij}+\sum_{j=0}^{k}p_{ji}-p_{ii}} \tag{6}$$

where k is the number of label categories, p_{ii} indicates the number of pixels that are correctly judged by category i, p_{ij} indicates the number of pixels that belong to category i and are misjudged as category j, and p_{ji} indicates the number of pixels that belong to category j and are judged as a category i. The value of MIoU ranges from 0 to 1, and the closer the value is to 1, the better the segmentation effect of the model.

The MIoU was calculated for core images on the validation set. When using U-Net, the MIoU was 79.02% and when using U-Net++, a high MIoU of 81.48% was achieved. The results of U-Net and U-Net++ in identifying pores and fractures was compared, as shown in Fig. 17. Although the U-Net network model can effectively identify pores, some pixels are still wrongly classified. The U-Net network model has a poor recognition effect on the edge areas such as pore boundaries and microfractures. For example, in Fig. 17(e), the region at the junction between organic and inorganic matter is incorrectly classified as an organic pore. By contrast, the segmentation results of the U-Net++ network are relatively more accurate: It can better identify different categories in the core images and performs better in handling details. In future research, this network can be applied to other data such as CT images to realize the identification of 3D pores and fractures once the required amount of data is collected.

For conventional sandstone, Saxena et al. (2021) used the U-Net network model to identify pores in sandstone thin sections with 92.2% accuracy. However, for shale reservoirs with complex pore structure, the accuracy of pore identification is

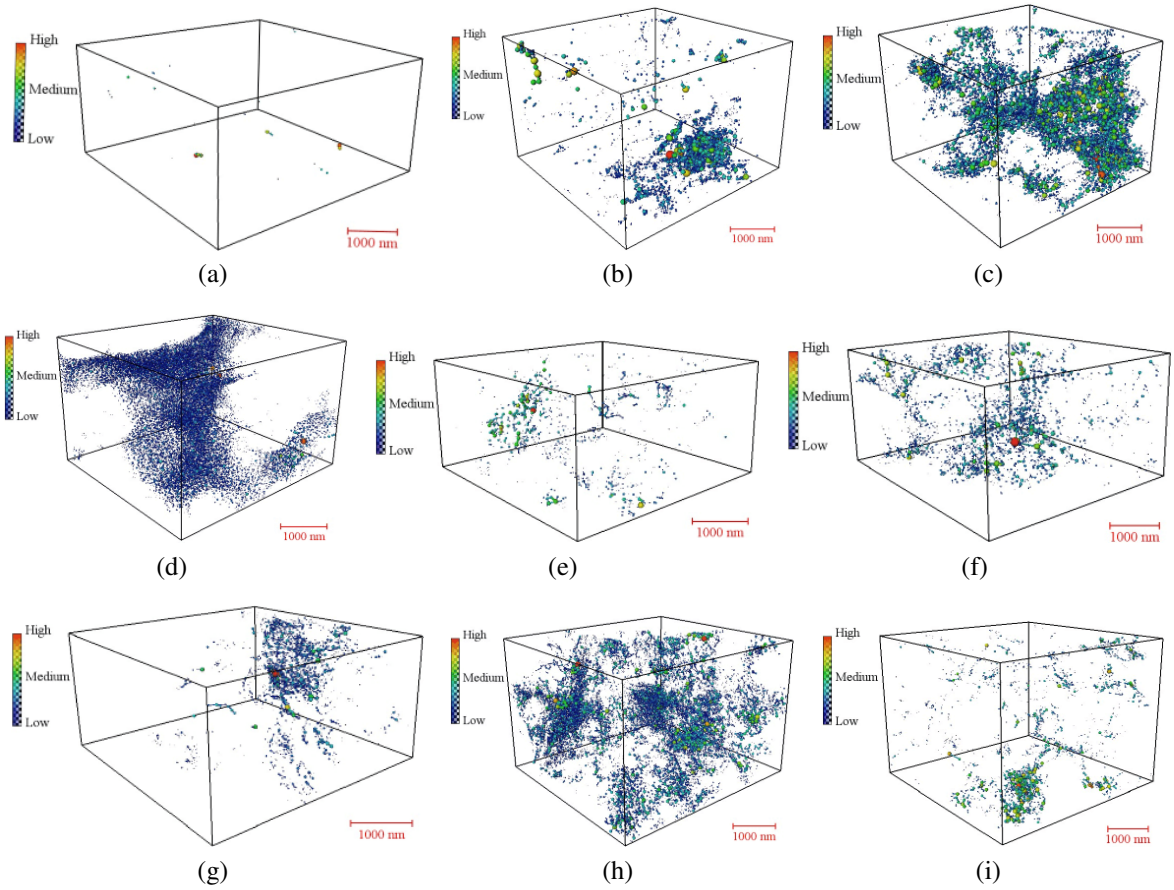

Fig. 14. Pore network model of FIB-SEM. (a) B1, (b) B3, (c) B9, (d) B12, (e) C1, (f) C6, (g) D4, (h) D6 and (i) Z15.

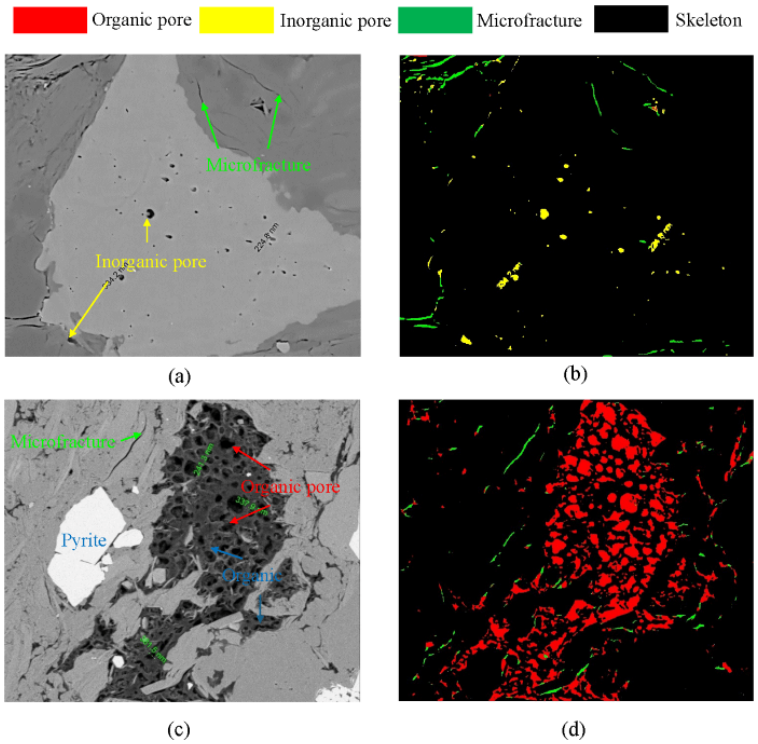

Fig. 15. Pore and fracture identification results of SEM images based on U-Net++. (a) Original SEM image of 136-3, (b) prediction image based on U-Net++, (c) original SEM image of 11-8 and (d) prediction image based on U-Net++.

Table 8. Organic pore parameters of SEM.

No.	n	ϕ (%)	r_m (nm)	a_r	G	ϕ_o (%)
135-1	4	0.03	172.98	0.599	0.8	1.41
136-3	7	0.03	83.1	0.49	0.75	4.43
135-2	308	4	54.86	0.51	0.61	90.77
11-6	26	0.88	97.86	0.44	0.63	32.16
11-8	860	11.3	154.87	0.6	0.67	100

Table 9. Inorganic pore parameters of SEM.

No.	n	ϕ (%)	r_m (nm)	a_r	G	ϕ_o (%)
135-1	223	1.82	156.81	0.67	0.77	98.59
136-3	112	0.74	123.28	0.63	0.77	95.57
135-2	89	0.41	31.13	0.6	0.74	9.23
11-6	/	/	/	/	/	/
11-8	/	/	/	/	/	/

relatively low. Chen et al. (2024) used the improved U-Net pore-net network model to accurately identify the pores in the shale SEM image, and the MIoU was around 80%; Liu et al. (2024) utilized the ShaleSeger network model to identify different types of pores in shale, and the MIoU was 72.28%. In this paper, the U-Net++ network was used to achieve automatic segmentation of different types of pores and fractures in shale reservoirs, which could accurately identify organic pores, inorganic pores and microfractures in the core. The MIoU was 81.2%, better than the U-Net model, mainly because the dense skip connection in the network structure can learn more details in the image.

4.2 Effect of pore structures on shale properties

Based on the extracted pore-fracture results, the study area exhibits extensive development of pores and fractures across various scales. At the mesoscopic scale, there is a significant development of millimeter-scale bedding fractures. The sedimentary environment of shale is diverse and the bedding structure is complex. A large number of mesoscopic fractures have developed in the Wufeng-Longmaxi Formation (Ou and Li, 2017). In the study area, the density of fractures in the $Long1_1^1$ sub-layer reaches more than 10 fractures/m. The bedding fractures can effectively expand the storage space and improve the connectivity between pores of different scales, which is helpful for shale oil and gas movement. Previous studies have shown that the development degree of bedding fractures is related to total organic carbon content; in layers with higher total organic carbon content, local abnormal high-pressure fluid will form more easily, resulting in larger fracture density (Ding et al., 2024).

At the microscopic scale, ranging from micrometers to nanometers, organic pores, inorganic pores and microfractures exhibit distinct developmental characteristics across various layers. Shale reservoirs are notably characterized by low porosity and permeability (Nie et al., 2016). The development of pores and fractures within the core contributes significantly to enhancing the reservoir properties (Chen et al., 2021). In the study area, micro-scale inorganic pores exhibit exceptional connectivity when fracture or large-sized pores are present, the micro-CT B1 develops a fracture, which has the best connectivity and the connected pores account for 99.62 % of the total pore volume. Large pores are developed in sample Z15, and the connectivity is second only to B1. In contrast, inorganic pores such as FIB-SEM B1 display poor connectivity at the nanoscale, while organic pores demonstrate superior connectivity (Borjigin et al., 2021). In the FIB-SEM B9, the organic pores clustered within the core exhibit enhanced connectivity in 3D structures compared to organic pores in 2D (Yang et al., 2020). In organic pores with larger pore sizes, pore connectivity is enhanced. In the core B1 of $Long1_2$, organic pores are notably scarce, contributing to low porosity. Conversely, the cores of $Long1_1$ exhibit a significant development of organic pores alongside microfractures. This formation displays high porosity, relatively large average pore sizes and good pore connectivity. In contrast, the core of the Wufeng Formation demonstrates relatively poor pore connectivity.

With the aid of the integrated multi-scale data processing workflow proposed in this paper, mesoscopic fractures, micropores and fractures, as well as nanopores and fractures can be obtained, which can help us understand the pore structure of the study area and provide quantitative data support for the selection of dominant sweet spots. According to the analysis, the pore structure characteristics of the study area show strong heterogeneity in the longitudinal direction. The mesoscopic low-angle fractures and organic matter pores are extensively developed in $Long1_1$, exhibiting excellent pore connectivity. The organic matter is hydrophobic, whereas minerals are hydrophilic. Under the same pore volume, a higher proportion of organic porosity implies a stronger adsorption capacity in the reservoir space (Borjigin et al., 2017). These characteristics contribute to better reservoir physical properties, providing favorable reservoir space for oil and gas accumulation. The data obtained by the workflow of this paper is consistent with the production data, which shows that $Long1_1$ is the sweet spot of the gas field.

4.3 Limitations of the workflow

This paper proposes a workflow that integrates multi-scale core data processing methods and achieves the accurate identification of pores and fractures for the extraction of their parameters. At the same time, this workflow still has some limitations. Firstly, for fracture identification in full-diameter core CT, the automatic fracture identification method mentioned in this paper can only distinguish a single fracture through the core. If there is a complex fracture network, fracture identification is difficult to achieve, and the real fracture opening and attitude cannot be currently obtained. Secondly, from the aspect of automatic pore identification, the deep learning method is used to successfully realize the automatic recognition of different types of pores in SEM

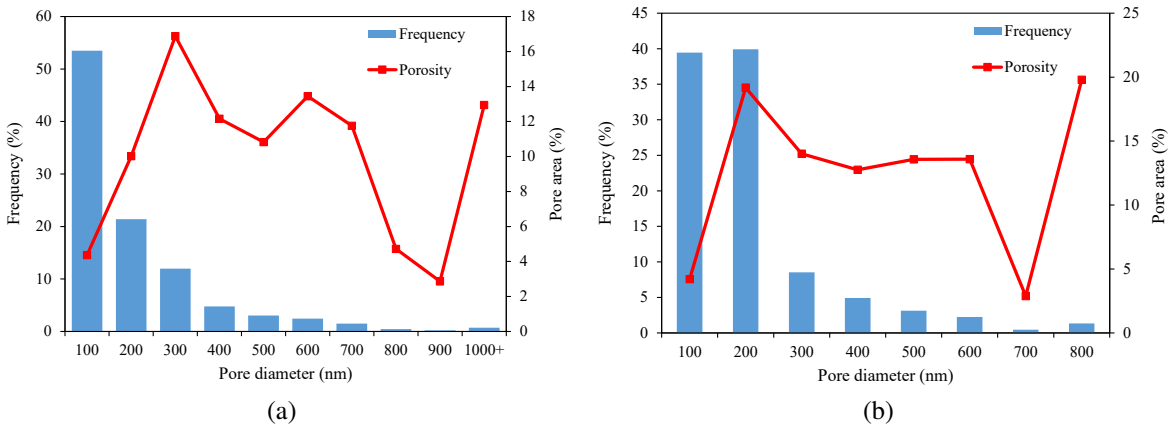

Fig. 16. Pore size distribution of different types of pores. (a) Pore size distribution of organic pores and (b) pore size distribution of inorganic pores.

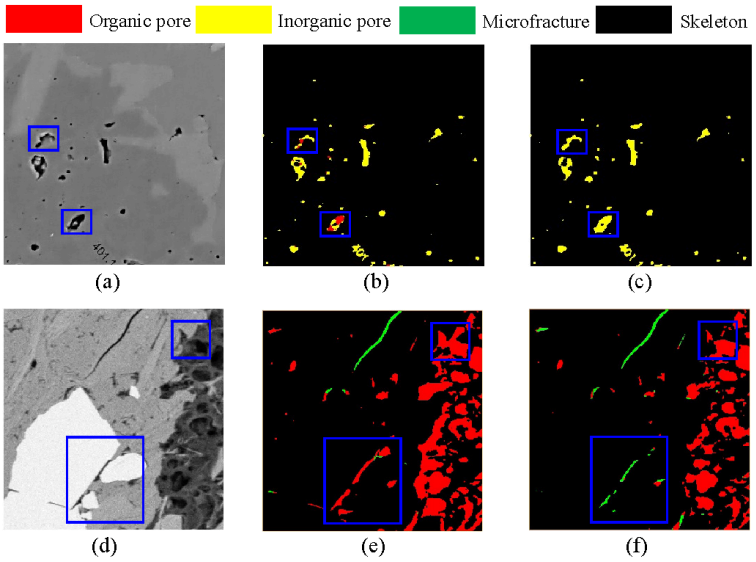

Fig. 17. Comparison of SEM image prediction results. (a) Original image, (b) prediction by U-Net, (c) prediction by U-Net++, (d) original image, (e) prediction by U-Net and (f) prediction by U-Net++.

images. Meanwhile, the extraction of pores from micro-CT and FIB-SEM images is still a manual task, so it is necessary to further study the automatic identification method of pores for different data. Finally, in view of the complex pore structure in shale reservoirs, analyzing the pore characteristics of different scales and realizing multi-scale fusion are further important directions for future research to achieve a deeper understanding of the reservoir space (Arif et al., 2021).

5. Conclusions

In this study, based on the collection of four different types of 2D and 3D multi-scale digital core images, including full-diameter core CT, micro-CT, FIB-SEM, and SEM, an integrated workflow was established for the identification of pores and fractures and the extraction of the characteristic parameters. Qualitative and quantitative characterizations of pores and fractures in the core images were conducted, summarizing the development characteristics of pores and fractures in different layers of a practical area. Finally, the advantages of the methods were discussed. The main conclusions are as follows:

1) By the integration of a variety of cross-scale core data processing methods, the presented workflow can identify the pores and fractures from mesoscopic to nanoscale and extract the parameters of pores and fractures.
2) Considering a practical scenario, the pore and fracture information of different shale formations in the study area were obtained. At the microscale, the porosity of the sample was higher when the number and size of inorganic pores were larger. It was established that the development of fractures and large-size pores contributes to pore connectivity. At the nanoscale, the more developed the organic pores, the larger the pore size and the better the pore connectivity. The pore fracture analysis results indicated widespread development of mesoscopic-microscopic pores and fractures in Long1_1, characterized

by high pore connectivity and superior reservoir physical properties, in line with the production data.

3) The results demonstrate that the workflow proposed in this paper can accurately characterize the pore and fracture features of reservoirs from meso- to microscale, providing essential guidance and support for the quantitative evaluation of pore and fracture characteristics in unconventional reservoirs.

However, it is important to note that the proposed workflow exhibits certain problems that warrant further investigations. Firstly, in full-diameter core CT, additional research should be conducted to identify fractures within complex fracture networks and accurately extract real fracture aperture and attitude. Secondly, the development of automated identification methods for pores and fractures based on diverse core data such as micro-CT and FIB-SEM holds significant promise. Nevertheless, the fusion of multi-scale pores and fractures from various core data represents a crucial avenue for future exploration, offering a foundation for a more comprehensive understanding of shale microstructures.

Acknowledgements

This study was financially supported by the Open Foundation of Cooperative Innovation Center of Unconventional Oil and Gas, Yangtze University (Ministry of Education & Hubei Province, No. UOG2024-20), the Open Fund of Key Laboratory of Exploration Technologies for Oil and Gas Resources (Yangtze University), the Ministry of Education (No. PI2023-03), and the open foundation of National Engineering Laboratory for Exploration and Development of Low-Permeability Oil & Gas Fields.

Conflict of interest

The authors declare no competing interest.

References

Arif, M., Mahmoud, M., Zhang, Y., et al. X-ray tomography imaging of shale microstructures: A review in the context of multiscale correlative imaging. International Journal of Coal Geology, 2021, 233: 103641.

Badrinarayanan, V., Kendall, A., Cipolla, R. Segnet: A deep convolutional encoder-decoder architecture for image segmentation. IEEE Transactions on Pattern Analysis and Machine Intelligence, 2017, 39(12): 2481-2495.

Borjigin, T., Lu, L., Yu, L., et al. Formation, preservation and connectivity control of organic pores in shale. Petroleum Exploration and Development, 2021, 48(4): 798-812.

Borjigin, T., Shen, B., Yu, L., et al. Mechanisms of shale gas generation and accumulation in the Ordovician Wufeng-Longmaxi Formation, Sichuan Basin, SW China. Petroleum Exploration and Development, 2017, 44(1): 69-78.

Byun, H., Kim, J., Yoon, D., et al. A deep convolutional neural network for rock fracture image segmentation. Earth Science Informatics, 2021, 14: 1937-1951.

Chen, X., Tang, X., He, R., et al. Intelligent identification and quantitative characterization of pores in shale SEM images based on pore-net deep-learning network model. Petrophysics, 2024, 65(2): 233-245.

Chen, Y., Jiang, C., Leung, J. Y., et al. Multiscale characterization of shale pore-fracture system: Geological controls on gas transport and pore size classification in shale reservoirs. Journal of Petroleum Science and Engineering, 2021, 202: 108442.

Ding, W., Wang, Y., Wang, S., et al. Research progress and insight on non-tectonic fractures in shale reservoirs. Earth Science Frontiers, 2024, 31(1): 297. (in Chinese)

Dong, H., Blunt, M. J. Pore-network extraction from micro-computerized-tomography images. Physical Review E - Statistical, Nonlinear, and Soft Matter Physics, 2009, 80: 036307.

Gao, S., Zhou, H., Gao, Y., et al. BayeSeg: Bayesian modeling for medical image segmentation with interpretable generalizability. Medical Image Analysis, 2023, 89: 102889.

Gobert, C., Kudzal, A., Sietins, J., et al. Porosity segmentation in X-ray computed tomography scans of metal additively manufactured specimens with machine learning. Additive Manufacturing, 2020, 36: 101460.

Goral, J., Deo, M. Nanofabrication of synthetic nanoporous geomaterials: From nanoscale-resolution 3D imaging to nano-3D-printed digital (shale) rock. Scientific Reports, 2020, 10(1): 21596.

Guo, Q., Wang, Y., Yang, S., et al. A method of blasted rock image segmentation based on improved watershed algorithm. Scientific Reports, 2022, 12(1): 7143.

Iqbal, M. A., Rezaee, R., Smith, G., et al. Shale lithofacies controls on porosity and pore structure: An example from Ordovician Goldwyer Formation, Canning Basin, Western Australia. Journal of Natural Gas Science and Engineering, 2021, 89: 103888.

Jiang, Z., Tahmasebi, P., Mao, Z. Deep residual U-net convolution neural networks with autoregressive strategy for fluid flow predictions in large-scale geosystems. Advances in Water Resources, 2021, 150: 103878.

Josh, M., Delle Piane, C., Esteban, L., et al. Advanced laboratory techniques characterising solids, fluids and pores in shales. Journal of Petroleum Science and Engineering, 2019, 180: 932-949.

Kumar, S., Mendhe, V. A., Kamble, A. D., et al. Geochemical attributes, pore structures and fractal characteristics of Barakar shale deposits of Mand-Raigarh Basin, India. Marine and Petroleum Geology, 2019, 103: 377-396.

Kwiecińska, B., Pusz, S., Valentine, B. J., et al. Application of electron microscopy TEM and SEM for analysis of coals, organic-rich shales and carbonaceous matter. International Journal of Coal Geology, 2019, 211: 103203.

Li, B., Nie, X., Cai, J., et al. U-Net model for multi-component digital rock modeling of shales based on CT and QEMSCAN images. Journal of Petroleum Science and Engineering, 2022, 216: 110734.

Li, B., Nie, X., Zhu, L., et al. Reconstruction of 3D shale

digital core based on generative adeversial neural networks with gradient penalty. Journal of Xi'an Shiyou University (Natural Science Edition), 2023a, 38(2): 53-60. (in Chinese)

Li, J., Song, Z., Wang, M., et al. Quantitative characterization of microscopic occurrence and mobility of oil in shale matrix pores: A case study of the Shahejie Formation in the Dongying Sag. Petroleum Science Bulletin, 2024, 9 (1): 1-20. (in Chinese)

Li, X., Li, B., Liu, F., et al. Advances in the application of deep learning methods to digital rock technology. Advances in Geo-Energy Research, 2023b, 8(1): 5-18.

Liu, Q., Ren, Y., Wang, W., et al. Intelligent representation method of shale pore structure based on semantic segmentation. Journal of Beijing University of Aeronautics and Astronautics, 2024, in press, http://doi.org/10.13700/j.bh.1001-5965.2024.0018. (in Chinese)

Liu, Q., Sun, M., Sun, X., et al. Pore network characterization of shale reservoirs through state-of-the-art X-ray computed tomography: A review. Gas Science and Engineering, 2023, 113: 204967.

Loucks, R. G., Reed, R. M., Ruppel, S. C., et al. Morphology, genesis, and distribution of nanometer-scale pores in siliceous mudstones of the Mississippian Barnett Shale. Journal of Sedimentary Research, 2009, 79(12): 848-861.

Masihi, M., Shams, R., King, P. R. Pore level characterization of Micro-CT images using percolation theory. Journal of Petroleum Science and Engineering, 2022, 211: 110113.

Mastalerz, M., Drobniak, A., Hower, J. C. Controls on reservoir properties in organic-matter-rich shales: Insights from MICP analysis. Journal of Petroleum Science and Engineering, 2021, 196: 107775.

Mastalerz, M., Hampton, L. B., Drobniak, A., et al. Significance of analytical particle size in low-pressure N_2 and CO_2 adsorption of coal and shale. International Journal of Coal Geology, 2017, 178: 122-131.

Mukherjee, M., Vishal, V. Gas transport in shale: A critical review of experimental studies on shale permeability at a mesoscopic scale. Earth-Science Reviews, 2023, 244: 104522.

Nie, X., Zou, C., Li, Z., et al. Numerical simulation of the electrical properties of shale gas reservoir rock based on digital core. Journal of Geophysics and Engineering, 2016, 13(4): 481-490.

Nie, X., Zou, C., Pan, L., et al. Fracture analysis and determination of in-situ stress direction from resistivity and acoustic image logs and core data in the Wenchuan Earthquake Fault Scientific Drilling Borehole-2 (50-1370 m). Tectonophysics, 2013, 593: 161-171.

Ou, C., Li, C. 3D discrete network modeling of shale bedding fractures based on lithofacies characterization. Petroleum Exploration and Development, 2017, 44(2): 336-345.

Ronneberger, O., Fischer, P., Brox, T. U-Net: Convolutional networks for biomedical image segmentation. Paper Presented at Medical Image Computing and Computer-Assisted Intervention - MICCAI 2015, Munich, Germany, 5-9 October, 2015.

Roslin, A., Marsh, M., Provencher, B., et al. Processing of micro-CT images of granodiorite rock samples using convolutional neural networks (CNN), Part II: Semantic segmentation using a 2.5D CNN. Minerals Engineering, 2023, 195: 108027.

Saxena, N., Day-Stirrat, R. J., Hows, A., et al. Application of deep learning for semantic segmentation of sandstone thin sections. Computers & Geosciences, 2021, 152: 104778.

Schlüter, S., Sheppard, A., Brown, K., et al. Image processing of multiphase images obtained via X-ray microtomography: A review. Water Resources Research, 2014, 50(4): 3615-3639.

Shelhamer, E., Long, J., Darrell, T. Fully convolutional networks for semantic segmentation. IEEE Transactions on Pattern Analysis and Machine Intelligence, 2017, 39(4): 640-651.

Slatt, R. M., O'Brien, N. R. Pore types in the Barnett and Woodford gas shales: Contribution to understanding gas storage and migration pathways in fine-grained rocks. AAPG Bulletin, 2011, 95(12): 2017-2030.

Valentine, B. J., Hackley, P. C. Scanning electron microscopic evaluation of broad ion beam milling effects to sedimentary organic matter: Sputter-induced artifacts or naturally occurring porosity? International Journal of Coal Geology, 2023, 277: 104348.

Wei, J., Zhang, A., Li, J., et al. Study on microscale pore structure and bedding fracture characteristics of shale oil reservoir. Energy, 2023, 278: 127829.

Wu, Y., Tahmasebi, P., Lin, C., et al. A comprehensive investigation of the effects of Organic-Matter pores on shale properties: A multicomponent and multiscale modeling. Journal of Natural Gas Science and Engineering, 2020, 81: 103425.

Yalamanchi, P., Datta Gupta, S. Estimation of pore structure and permeability in tight carbonate reservoir based on machine learning (ML) algorithm using SEM images of Jaisalmer sub-basin, India. Scientific Reports, 2024, 14(1): 930.

Yang, W., Cai, J., Wang, Q., et al. The controlling effect of organic matter coupling with organic matter porosity on shale gas enrichment of the Wufeng-Longmaxi marine shale. Petroleum Science Bulletin, 2020, 5(2): 148-160. (in Chinese)

Yin, S., Feng, K., Nie, X., et al. Characterization of marine shale in Western Hubei Province based on unmanned aerial vehicle oblique photographic data. Advances in Geo-Energy Research, 2022, 6(3): 252-263.

Zhou, Y., Chang, D., Zheng, J., et al. A fast workflow for automatically extracting the apparent attitude of fractures in 3-D digital core images. Processes, 2023, 11(9): 2517.